



Corrosion Inhibition of Sodium Phosphate for Coarse and Near Ultrafined-Grain Mild steel surface

Kazem Sabet Bokati¹, Changiz Dehghanian^{*1}

¹School of Metallurgy and Materials Engineering, College of Engineering, University of Tehran, P.O. Box 11155-4563, Tehran, Iran.

Received: 12 March 2017; Accepted: 20 June 2017

* Corresponding author email: cdehghan@ut.ac.ir

ABSTRACT

An ultrafine grain surface layer with average crystallite size of 28 nm was produced on annealed mild steel through a wire brushing process. The effects of grain size reduction on the inhibition performance of sodium phosphate were investigated using polarization and electrochemical impedance spectroscopy (EIS) measurements. The crystal grain size of wire brushed surface was analyzed by X-ray diffractometry (XRD) and field emission scanning electron microscopy (FESEM). The electrochemical tests were conducted in artificial sea water (ASW) in the presence and absence of 250 mg/lit sodium phosphate (SP). The wire brushed surface indicated considerable deformed plastic flows and high surface roughness. Due to the accumulated strains, a deformed layer with thickness of $20 \pm 5 \mu\text{m}$ was produced and the crystal grain size of severe deformed zone was about 28 nm. Wire brushed surface increased uniform corrosion rate of mild steel due to enhanced surface roughness and preferential sites to adsorption of corrosive ions. However, the wire brushed surface showed a positive effect on inhibition performance of sodium phosphate. The electrochemical results revealed that average inhibition efficiency increased from 65 to about 80 percent in ASW solution containing 1.5 mM Na_3PO_4 for coarse grained samples in comparison to that of ultra-fined grain samples respectively. The wire brushing process encouraged passivity on the surface in SP-containing solution due to a high density of nucleation sites which increased the adsorption of phosphate ions leading to a high fraction of passive layers and low corrosion rates.

Keywords: Mild steel, Ultrafine grain surface, Inhibition performance, Sodium phosphate.

How to cite this article:

Sabet Bokati K, Dehghanian C. Corrosion Inhibition of Sodium Phosphate for Coarse and Near Ultrafined-Grain Mild steel surface. *J Ultrafine Grained Nanostruct Mater*, 2017; 50(1):33-42.

DOI: [10.7508/jufgnsm.2017.01.05](https://doi.org/10.7508/jufgnsm.2017.01.05)

1. Introduction

It is well known that most failures of materials arise from the surface. Fatigue fracture, wear and corrosion are important examples of engineering failures which are very sensitive to the properties of the material's surface [1]. Properties of metal surface were influenced by a various types of surface structure consisted of complex crystal faces, edges, corners, boundaries and disturbed layer. The high volume fraction of grain boundaries in metal structures results in positioning of atoms in

grain boundaries. An increase in volume fraction of grain boundaries that are not part of original crystalline lattice resulted in an increase in surface energy and correspondingly accelerated reaction rates on metal surface [2].

The corrosion resistance of a metal in a corrosive environment is attributed to the formation of a protective passive film on its surface. Zhao Cheng et al [3] claimed that nanocrystallization of carbon steel by wire-brushing improved its corrosion resistance due to enhanced oxide film formation,

although this process cause an increase in surface roughness. Song et al. [4] reported that surface nanocrystallization of rebar through wire-brushing process improved corrosion resistance in chloride containing saturated $\text{Ca}(\text{OH})_2$ solution due to enhanced passivation performance. Afshari and Dehghanian investigated the corrosion behavior of nanocrystalline iron made by electrodeposition technique and compared that with a polycrystalline annealed iron in alkaline solution. They reported that nanocrystalline iron showed improved corrosion resistance [5]. Ralston and Birbilis [6] claimed that improved corrosion resistance from grain refinement is generally attributed to an improvement in passive film stability, which can be the result of increased rates of diffusion in nano- or fine-grained structures. On the other hand, increased rates of corrosion as grain size decreases are attributed to passive film destabilization. According to these reports the corrosion behavior varies among surface structure and corrosion environment.

The use of corrosion inhibitors is one of the promising ways to decrease the corrosion rate of metals in aggressive environments [7]. The effectiveness of a corrosion inhibitor depends on its ability to adsorb onto metal surface to form a protective layer. Adsorption of an inhibitor is influenced by the structure of the inhibitor, surface charge of the metal, and the type of electrolyte [8]. Shen et al. [9] investigated the inhibiting effect of thiourea on the corrosion of bulk nanocrystalline and coarse-grained industrial pure iron in hydrochloric acid solution and observed that the nanocrystalline structure displayed better corrosion resistance in both inhibited and uninhibited acid. However, Oguzie et al. [10] reported that nanocrystalline iron in sulfuric acid was more susceptible to corrosion than that of polycrystalline one, although the inhibition performance of amino acid cysteine was more pronounced for nanocrystalline sample. Pour-Ali et al. [11] indicated that surface nanocrystallization of mild steel through wire brushing improved the inhibition performance of 3-amino-1,2,4-triazole inhibitor in HCl solution due to its progress in adsorption of inhibitor molecules on surface. Afshari and Dehghanian [12,13] investigated the influence

of nanocrystalline state of iron on the inhibition effect of sodium nitrite and sodium benzoate in near-neutral aqueous solution and their results revealed that inhibitor performance increased as the grain size shifted from microcrystalline to nanocrystalline due to an increase in surface energy which encouraged adsorption of inhibitor on the surface. In agreement with the change in surface activity, the SNC treatment may affect the extent of adsorption and surface coverage of corrosion inhibitors on the metal surface.

It is common to produce an ultrafine-grained surface through severe plastic deformation (SPD) processes. Among SPD processes, wire brushing is relatively simple, flexible and applicable for different classes of materials. Wire brushing will result in extreme grain refinement at the surface without changing the microstructure of steel matrix [4]. This technique is also capable of modifying the surface microstructure which in turn, helps in more effective adsorption of corrosion inhibitors and an improvement in coating adhesion [14]. The objective of this work is to study the effect of near surface severe plastic deformation (NS-SPD) process on corrosion behavior of mild steel and inhibition performance of sodium phosphate for steel in artificial sea water. For this purpose, wire brushing was used to achieve a surface layer with ultrafine grains. Field emission scanning electron microscopy (FESEM), optical microscopy (OM) and X-ray diffraction (XRD) were used to characterize the surface. Afterwards, the corrosion inhibition of sodium phosphate on mild steel coupons with coarse- and ultrafine-grained surfaces was evaluated by potentiodynamic polarization and electrochemical impedance spectroscopy (EIS) in artificial sea water.

2. Materials and Experimental Procedure

Table 1 shows Coarse grained (CG) sample which was prepared by annealing process for mild steel panels. Near surface ultrafine grained (NS-UFG) specimen was produced by wire brushing of annealed sample. The surface of the annealed samples were initially abraded with silicon carbide papers starting from 120 to 600 grit size and then degreased by acetone. Afterward, the samples were wire-brushed at room temperature for the near

Table 1- Chemical composition of mild steel

Elements	Fe	C	Al	Si	P	S	Cu
(Wt %)	99.21	0.14	0.04	0.05	0.03	0.03	-

surface severe plastic deformation (NSSPD). A 304 stainless-wire brush was driven by a drill machine at room temperature. The rotating wire-brush was pressed on the surface of the samples, and it was moved in both directions along the longitudinal direction (LD) of the sheets at a rotating speed of 12000 rpm and load of 2 kgf. The wire brushing process was repeated up to about five times.

The phase composition of samples and grain size of the wire-brushed specimen was analyzed by X-ray diffractometry (XRD). A Philips X'Pert-Pro instrument was used in X-ray diffraction studies which was operated at 40 kV and 30 mA with CuK α radiation ($\lambda=0.154$ nm). The broadening of full width at half-maximum of the peak can be attributed to reduction of crystal grain size. An average grain size was calculated by Scherrer-Wilson equation [15].

$$B_r \cdot \cos\theta = \frac{K\lambda}{D} + \eta\sin\theta \quad (\text{Eq. 1})$$

Where D is the average grain size, λ is the wavelength of the X-ray, θ is the Bragg angle for the peak, and β_r is the intrinsic profile FWHM. The β parameter was calculated using the Gaussian-Gaussian (GG) relationship:

$$\beta_{\text{exp}}^2 = \beta^2 + \beta_{\text{inst}}^2 \quad (\text{Eq. 2})$$

Where β_{inst} and β_{exp} represent the full width of the diffraction line measured at FWHM of instrumental and experimental profiles, respectively. By plotting $\beta\cos\theta$ vs. $\sin\theta$ a straight line with an intercept equal to $K\lambda/D$ will be obtained. An annealed mild steel with average grain size of 80 μm was used as reference sample to determine instrumental broadening corrections. The average crystal size of 28 nm was obtained for the treated samples. The thickness of the deformation affected zone for the wire brushed sample was determined by IM-20 Inverted Metallurgical Microscope. IM-20 Inverted Metallurgical Microscope was also used to analyze the surface microstructure of annealed sample. The surface morphology of samples was analyzed by field emission scanning electron microscopy (ZIESS SIGMA VP). Before and after the wire brushing treatments, the surface roughness was measured by using a HOMMEL tester (Turbo Roughness V3.34). The R_a , R_z and R_{max} of each

specimen is the average values of 3 measurements.

Electrochemical tests for the samples were conducted in artificial sea water (Table 2) in the presence and absence of 250 mg/lit sodium phosphate (Na_3PO_4) inhibitor using a conventional three-electrode cell. A saturated calomel electrode and platinum foil were used as a reference electrode and an auxiliary electrode, respectively. Annealed and wire brushed mild steel samples were used as working electrodes. Firstly a copper wire was brazed to the specimens and then they were cold mounted to seal their edges and backsides. Prior to measurements, the working electrode was allowed to stabilize in the electrolyte for 1 and 24 hours. The surface area exposed to corrosive electrolyte was 1 cm^2 . The samples were polarized from -0.3 V vs. its open circuit potential (OCP) to a potential of 0.6 V vs. SCE with a scan rate of 1 mV/s using potentiostat Model 273 (EG and G) with "Softcorr 352" software. EIS measurements were also conducted by Solartron SI-1260 at OCP after potential stabilization. The applied potential amplitude was chosen to be 10 mV with frequency ranging from 0.01 Hz to 100 KHz. The experimental data were simulated with an equivalent circuit using "ZView2" software. To calculate inhibition efficiency (η) from polarization measurements equation 3 was used [13]:

$$\eta (\%) = J_0 - J_i / J_0 \times 100 \quad (\text{Eq. 3})$$

where J_i and J_0 are the corrosion current densities in presence and absence of corrosion inhibitor, respectively.

Inhibition efficiency was also calculated from EIS measurements by the following equation [16-17]:

$$\eta (\%) = R_{\text{ct}(i)} \cdot R_{\text{ct}(0)} / R_{\text{ct}(0)} \times 100 \quad (\text{Eq. 4})$$

Where $R_{\text{ct}(0)}$ and $R_{\text{ct}(i)}$ are the charge transfer resistance in the absence and presence of corrosion inhibitor, respectively.

3. Results and discussion

Figure 1 indicate a cross sectional optical microscopic observation of wire brushed mild steel sample. The microstructure morphology of treated zone with a thickness of about 20 μm differs from matrix. Moreover, the grain boundaries in the treated surface layer could not be identified as in

Table 2- Chemical composition of artificial sea water (ASW) [16]

Compound	NaCl	MgCl ₂	CaCl ₂	KCl	Na ₂ SO ₄	NaHCO ₃	KBr
Concentration (g/L)	24.53	5.2	1.16	0.7	4.09	0.20	0.10

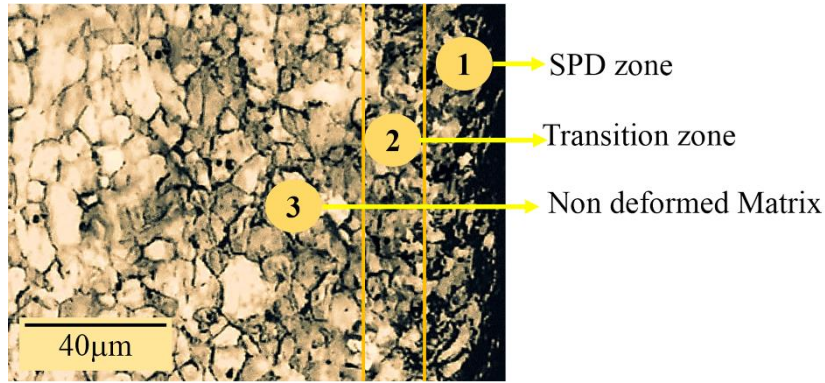


Fig. 1- Cross sectional OM micrograph of NS-UFG sample.

the matrix which is an evidence for severe plastic deformation of surface. The surface deformation layer thickness in the entire mild steel surface is not uniform from place to place ($\pm 5 \mu\text{m}$), indicating the heterogeneity of plastic deformation induced by wire brushing both within and between grains [17].

XRD patterns of samples before and after the NS-SPD process are shown in Fig.2. The broadening of peaks in the wire brushed state may be an indication of grain refinement to an ultrafine size. The NS-SPD process caused appearance of characteristic peaks of iron oxide in XRD pattern, indicating oxidation of steel surface during treatment. The average crystal size of 28 nm was obtained for NS-UFG sample. The wire-brushing severely scratches and stirs the surface layers of metals. In this case, a complicated metal flow is induced there that gives rise to very large amounts of plastic strain into the surface layer. According to the literature [3,4,18] the NS-SPD process by wire brushing leads

to formation of a nanocrystalline surface which is attributed to ultrafine grain subdivision and recovery as well.

The FESEM and optical images of the CG and NS-UFG mild steel samples are shown in Figure 3. According to this Figure, wire brushing process drastically changed the surface morphology of mild steel. Obviously, the structure of annealed sample indicates a coarse grain structure, while fine grains are formed on the surface of NS-SPD processed sample due to severe plastic deformation which was occurred in the wire-brushed zone. Moreover, the wire brushing process caused a significant increase in surface roughness. Table 3 represents the surface roughness test results. The untreated specimen has a roughness average (R_a) of 0.48 μm , a 10-point height (R_z) of 3.93 μm and a maximum peak to valley roughness height (R_{max}) of 5.32 μm . The NS-SPD process, increased the R_a , R_z and R_{max} values significantly.

Potentiodynamic polarization curves of CG

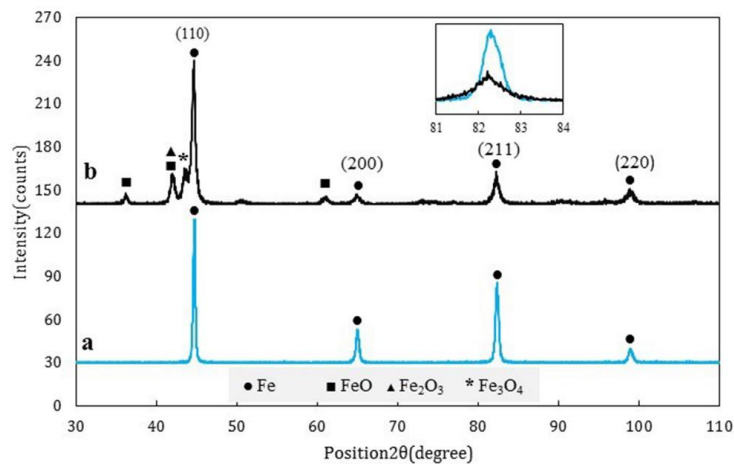


Fig. 2- XRD pattern of (a) CGMS and (b) NS-UFGMS.

Table 3- Surface roughness test results for CGMS, NS-UFGMS samples

Sample	R_a (μm)	R_z (μm)	R_{max} (μm)
CGMS	0.48 ± 0.02	3.93 ± 0.06	5.32 ± 0.09
NS-UFGMS	1.96 ± 0.05	11.38 ± 0.05	15.97 ± 0.07

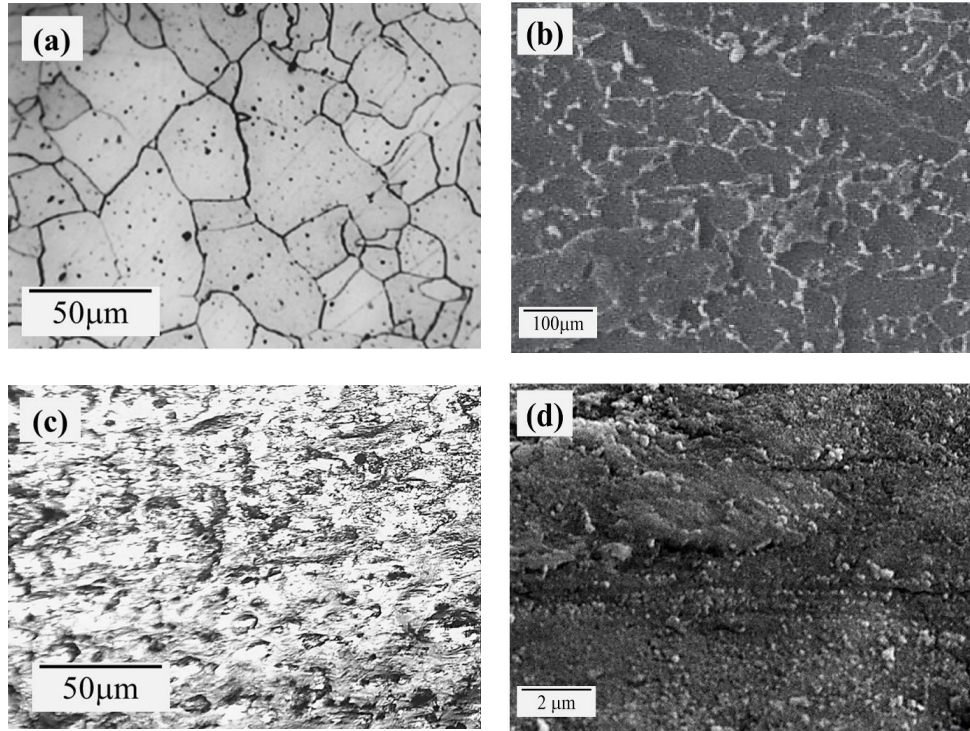


Fig. 3- Optical microscopy and SEM micrographs of a, b) CG and c, d) NS-UFG mild steel samples.

and NS-UFG samples in the artificial sea water with and without SP are shown in Figure 4. Table 4 represents the values for corrosion current densities, corrosion potentials and inhibition efficiencies obtained from the polarization curves in Fig.4. The polarization curves of wire brushed sample in artificial sea water exhibited more active corrosion potential and higher corrosion rate compared to that of annealed sample. Nano

crystallized materials have large quantities of grain boundaries which act as preferential paths to accelerate corrosion rate due to the large numbers of nano electrochemical cells within the matrix [12]. However, more surface roughnesses for treated specimens are another reason to be considered for low corrosion resistance. In fact, the practical area for corrosion per unit area will be increased by an increase in surface roughness

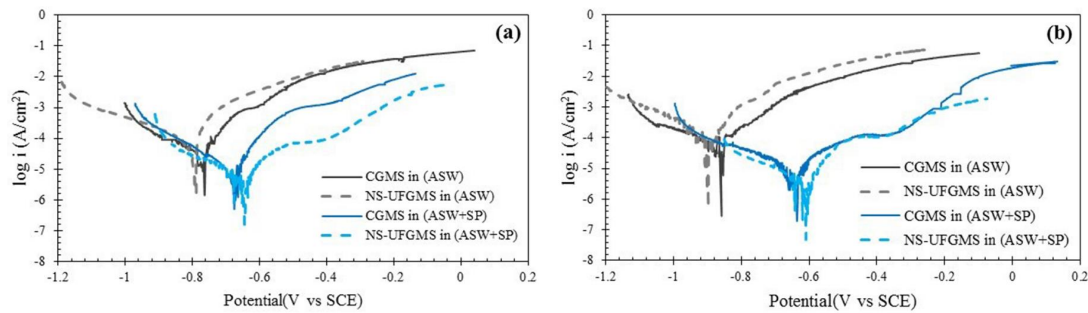


Fig. 4- Potentiodynamic polarization curves for CG and NS-UFG mild steel samples in artificial sea water without and with SP inhibitor after (a) 1 hour and (b) 24 hours immersion time.

Table 4- Parameters obtained from polarization curves for CG and NS-UFG samples in ASW in the presence and absence of SP inhibitor after a) 1 and b) 24 hours immersion

Solution	pH	Time (h)	Sample	E_{corr} (mV)	J_{corr} ($\mu\text{A}/\text{cm}^2$)	η (%)
ASW	7.6	1	CGMS	-763	17.3	-
			NS-UFGMS	-791	25.1	-
		24	CGMS	-647	7.9	-
			NS-UFGMS	-634	4.9	-
ASW + 1.5 mM SP	8	1	CGMS	-836	22.5	53
			NS-UFGMS	-870	33.3	80
		24	CGMS	-625	5.7	75
			NS-UFGMS	-609	3.1	89

[20], [21]. However, addition of SP inhibitor to the corrosive solution caused polarization curves to exhibit lower current densities as shown in Table 4. Interestingly, at initial time of immersion, the inhibitive performance of SP was more pronounced for ultrafine-grained specimen, probably due to more inhibitor adsorption on the surface.

The longer immersion times increased inhibition efficiency of SP for both CG and UFG mild steel samples. This was confirmed by a positive shift in corrosion potential and a slight decrease in corrosion current densities for specimens which were exposed to solution containing SP for 24 h. More coverage, and growth of protective layer on mild steel surface in SP-containing solution with an increase in exposure time resulted in an improved protection. A decrease in anodic current density

together with a positive shift in potential towards more noble values indicate that anodic inhibition mechanism is dominant for SP. Beside the positive effect of NS-SPD process on adsorption of phosphate ions on the samples, the good stability of protective layer formed on the surface made SP to provide a good inhibition performance for treated sample.

Figure 5 presents the EIS spectra for CG and NS-UFG samples in artificial sea water in the presence and absence of inhibitor. The impedance plot for the corrosion of mild steel in inhibitor-free solution showed just one time constant, while two time constants were observed for solution containing SP inhibitor. The equivalent circuit shown in Figure 6a, was used to simulate the impedance plots and calculate electrochemical parameters for corrosion

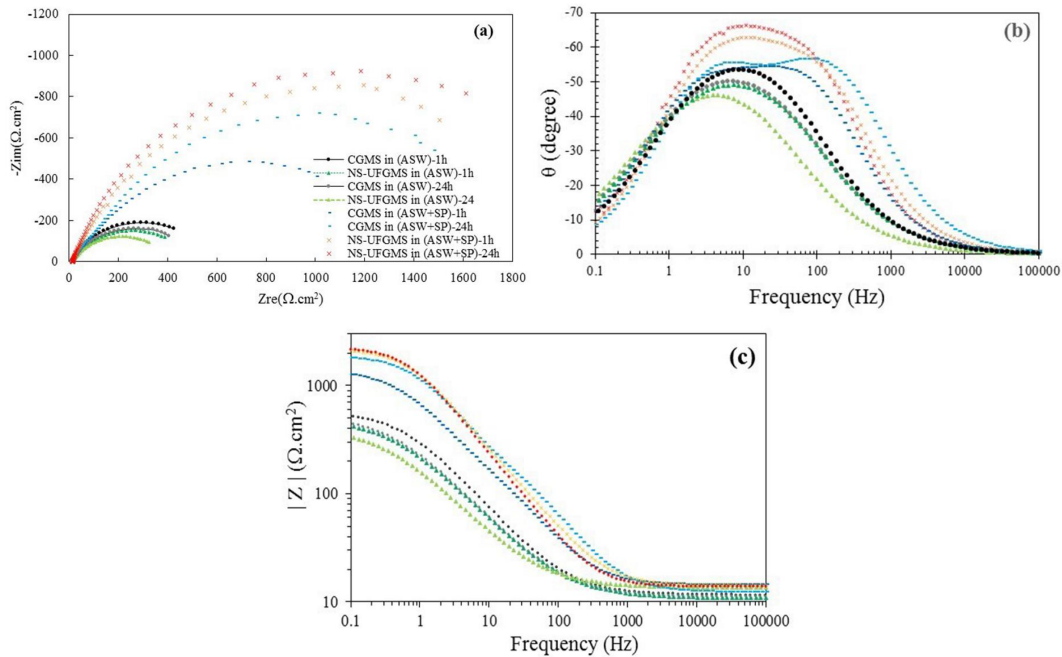


Fig. 5- (a) Typical Nyquist and (b) phase angle vs. frequency plots of the CG and NS-UFG mild steel samples after 1 and 24 hours immersion in artificial sea water without and with SP inhibitor.



Fig. 6- The equivalent circuits used to simulate corrosion behavior of samples in a) inhibitor free and b) SP-containing artificial sea water using EIS measurement.

Table 5- Characteristic parameters obtained from EIS measurements for CG and NS-UFG mild steel immersed in ASW solution in the absence and presence of 300mg/lit SP for 1 and 24 hours

Solution	pH	Time (h)	Sample	R_s	CPE_{pl}		R_{pl}	CPE_{dl}		R_{dl}	η (%)
					n_{pl}	Y_{pl}		n_{dl}	Y_{dl}		
ASW	7.6	1	CGMS	11.4	-	-	-	0.75	615	566	-
			NS-UFGMS	10.8	-	-	-	0.70	893	483	-
		24	CGMS	11	-	-	-	0.71	914	512	-
			NS-UFGMS	11.5	-	-	-	0.77	1318	451	-
ASW + 1.5mM SP	8	1	CGMS	14.3	0.84	139	241	0.75	198	1148	50
			NS-UFGMS	13.4	0.87	93	351	0.82	59	1743	72
		24	CGMS	12.2	0.84	75	325	0.86	78	1536	63
			NS-UFGMS	13.9	0.89	86	372	0.83	46	1913	76

* $R(\Omega.cm^2)$, $Y(\mu F.cm^{-2}.s^{n-1})$

samples in artificial seawater. In this case, the one-time constant relates to corrosion reactions on the surface; R_s and R_{ct} represent the solution and charge transfer resistance, CPE_{dl} parameter corresponds to non-ideal capacitive behavior of the metal/solution interface which is attributed to the inhomogeneity in the conductance, the surface roughness or adsorption reactions [19,20]. Y represents admittance of CPE and relates to the reactive surface area and thus is a measure of corrosive solution permeation into the protective layer. n is the exponent of CPE and an exponent of less than 1 indicates the dispersion of capacitor effects [21,22].

The impedance plots for corrosion behavior of samples in inhibitor containing solutions, showed two time constants. The equivalent circuit of Fig. 6b is used for simulation of the data [19,23]. In this case, CPE_{pl} and R_{pl} parameters reflect the capacitive behavior and resistance of the protective layer formed by inhibitors, respectively [20,22]. The electrochemical parameters were extracted from fitting experimental data to the proposed equivalent circuits Fig.6 as listed in Table 5.

It was found that R_{ct} values for mild steel increased in the presence of SP inhibitor. An increase in the exposure time for mild steel in SP-containing solution from 1 to 24 hours increased R_{ct} values. Moreover, an increase in the height of phase angle was noticed with increasing immersion time, which indicates lower tendency for current to pass through the defects in protective layer [21]. An increase in the radius of capacitive loop and also the maximum of phase angle with immersion time

indicate a progress in inhibition, probably due to more coverage and growth of protective layer on the surface. The larger radius in low frequency capacitive loop and higher maximum value for phase angle in ultrafine grained sample in SP-containing solution compared to that of coarse grained one indicate a positive effect for surface treatment by inhibitive performance of sodium phosphate.

Figure 7 represent a Schematic plot of layer formed on the surface for coarse and fine grain mild steel immersed in artificial sea water in the presence and absence of SP inhibitor. In the absence of corrosion inhibitor (Figure 7a and 7b) a permeable protective layer consisting of $FeCl$, $CaCO_3$ and $Mg(OH)_2$ products with a weak protective nature formed on mild steel surface [24,25]. In this case, the NS-SPD process caused a decrease in corrosion resistance due to the high grain boundary density which provided more active sites for corrosion attacks. In reality, plastic deformation leads to an increase in dislocation density which in turn increases the corrosion rate by providing more sites at which electrons are more active [26]. The higher surface roughness produced by NS-SPD processed specimen also increased the electrochemical reaction rates. An increase in surface roughness increased the fluctuation of the electron work function which promoted formation of corrosion cell and accordingly acceleration of corrosion rate. The presence of some peaks and valleys on a rough surface increased the difference between EWF in different regions of surface, so that a peak with lower EWF is more anodic than

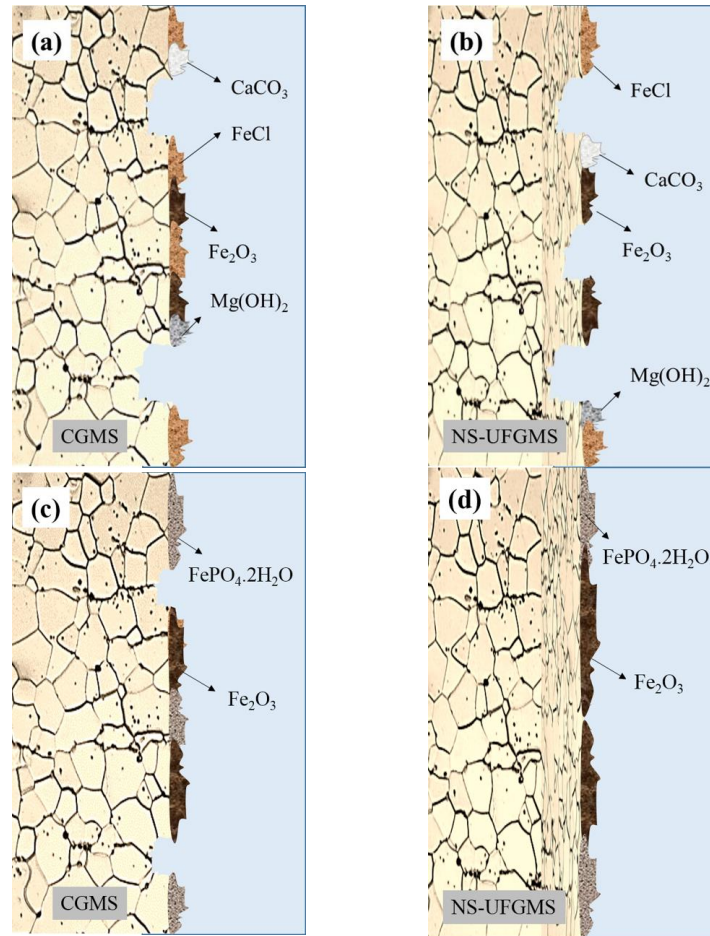


Fig. 7- The proposed models of protective layer formed on CG and NS-UFGMS samples in a, b) ASW, c,d) ASW+SP.

that of the region in valley. Therefore, the surface roughness promoted formation of corrosion cell and acceleration of corrosion surface [27].

In the presence of a SP inhibitor, a dense, more compact and low permeable resistive layers formed on mild steel surface (Figure 7c and 7d). An increase in inhibition efficiency with immersion time indicates low permeability of resistive layers. The corrosion inhibition of the phosphate ions may be due to the specific complex on steel which was precipitated from metal phosphate in the solution. An accumulation of a poorly soluble iron phosphate on the steel surface creates a favorable conditions for oxide formation. The dissolved oxygen produces a defective thin film of γ -Fe₂O₃. The phosphate ions fill the voids and accelerate film growth. These blocked voids prevent further diffusion of Fe²⁺ ions from the metal surface [28]. It is claimed that in the presence of Na₃PO₄ a protective film consists of a mixture of γ -Fe₂O₃ and FePO₄·2H₂O is formed on

the surface [29]. Phosphate ions may incorporate into electrical double layer at the metal surface. It is also possible that phosphate ions may fill the voids in the adsorbed film and increase the protective film growth due to void blocking which prevents further diffusion of Fe²⁺ ions from the metal surface [28]. According to the obtained results, the NS-SPD process encouraged passivity on the surface in SP-containing solution due to a high density of nucleation sites which increased the adsorption of phosphate ions leading to a high fraction of passive layers and low corrosion rates.

The ability of an inhibitor to be adsorbed on the metal surface depends on the electrostatic interaction between the metal and the inhibitor. In this case, the surface of crystalline lattice defects, grain boundaries and dislocations inside the grains are preferential sites to interact with inhibitor [13]. The grain boundaries in a SPD processed surface are not usually in a state of equilibrium; this may result

in a larger driving force for formation of protective film [30]. Therefore, the NS-SPD processed surface has a high density of active sites for inhibitor adsorption, which accelerates the formation of protective layer in inhibitor containing solution. Moreover, the SPD treated surface contains a considerable volume fractions of interphase or grain boundary regions and as a result a large specific interphase energy. The excess free energy (G_{excess}) per unit volume of a nanocrystalline solid has a form shown below:

$$G_{\text{excess}} = \alpha d^{-1} + \beta d^{-2} + \gamma d^{-3} \quad (\text{Eq. 5})$$

where d is the grain diameter, α , β , and γ are constant incorporating geometrical factors, α being proportional to the grain boundary excess free energy per unit area, β is junction energy per unit length, and γ is vertex energy [13,31]. The large specific surface areas of nanocrystalline and concomitantly large specific surface energy with surface sensitive properties (like catalytic activity) are enhanced [32,33] whereas the surface energy which is the driving force for the process are facilitated [13]. Depending upon the stability of protective layer, the NS-SPD process could increase or decrease the inhibition performance of inhibitor. At initial time of immersion, the inhibition performance of SP was more pronounced for ultrafine grained samples. Since the protective layer formed on mild steel in SP containing solution provided a good stability during immersion time, the catalytic effect of surface treatment on the adsorption of phosphate ions caused higher inhibition performance for ultrafine grained samples in comparison to coarse grained ones.

4. Conclusion:

An ultrafine grained surface layer was achieved via wire brushing process. The wire brushed surface indicated marked deformed plastic flows and increased surface roughness. A deformed layer with thickness of $20 \pm 5 \mu\text{m}$ was generated and the crystal grain size of severe deformed zone was about 28 nm. A higher current density, more active corrosion potential, a higher corrosion rate and a higher surface roughness were found for ultrafine grained mild steel surface in comparison to the coarse grained surface. This is directly related to high grain boundary density which provide more active sites for corrosion attacks. However, in the presence of sodium phosphate, the NS-UFG sample indicated a superior corrosion resistance compared

with the CG one. The NS-UFG mild steel had a high density of nucleation sites for encouraging adsorption of phosphate ions, which leads to a high fraction of passive layers and lower corrosion rates.

References:

1. Davis JR . Surface engineering for corrosion and wear resistance. ASM international, 2001.
2. Miyamoto H. Corrosion of Ultrafine Grained Materials by Severe Plastic Deformation. an Overview. *Materials Transactions*. 2016;57:559–572.
3. Cheng Z, Dan S, Jiang J, Jiang J, Kai YOU. Microstructure Characteristic and Electrochemical Corrosion Behavior of Surface Nano-crystallization Modified Carbon Steel. *Journal of Iron and Steel Research, International*. 2016;23:1281–1289.
4. Song D, Ma A, Sun W, Jiang J, Jiang J, Yang D, Guo G. Improved corrosion resistance in simulated concrete pore solution of surface nanocrystallized rebar fabricated by wire-brushing. *Corrosion Science*. 2014;82:437–441.
5. Afshari V, Dehghanian C. Effects of grain size on the electrochemical corrosion behaviour of electrodeposited nanocrystalline Fe coatings in alkaline solution, *Corrosion Science*. 2009;51:1844–1849.
6. Ralston KD, Birbilis N. Effect of grain size on corrosion: a review. *Corrosion*. 2010;66:75005.
7. Sastri VS. Green corrosion inhibitors: Theory and practice. John Wiley & Sons. 2012.
8. Yagasaki T, Matsumoto M, Tanaka H. Adsorption mechanism of inhibitor and guest molecules on the surface of gas hydrates. *Journal of the American Chemical Society*. 2015;137:12079–12085.
9. Shen CB, Wang SG, Yang HY, Long K, Wang FH. Corrosion and corrosion inhibition by thiourea of bulk nanocrystallized industrial pure iron in dilute HCl solution. *Corrosion Science*. 2006;48:1655–1665.
10. Oguzie EE, Wang SG, Li Y, Wang FH. Corrosion and corrosion inhibition characteristics of bulk nanocrystalline ingot iron in sulphuric acid. *Journal of Solid State Electrochemistry*. 2008;12:721–728.
11. Pour-Ali S, Kiani-Rashid A, Babakhani A. Improved corrosion inhibition of 3-amino-1, 2, 4-triazole on mild steel electrode in HCl solution using surface nanocrystallization. *International Journal of Materials Research*. 2016;107:1031–1040.
12. Afshari V, Dehghanian C. The effect of pure iron in a nanocrystalline grain size on the corrosion inhibitor behavior of sodium benzoate in near-neutral aqueous solution. *Materials Chemistry and Physics*. 2010;124:466–471.
13. Afshari V, Dehghanian C. Inhibitor effect of sodium benzoate on the corrosion behavior of nanocrystalline pure iron metal in near-neutral aqueous solutions. *Journal of Solid State Electrochemistry*. 2010;14:1855–1861.
14. Kitahara H, Yada T, Tsushida M, Ando S. Microstructure and evaluation of wire-brushed Mg sheets. *Procedia Engineering*. 2011;10:2737–2742.
15. Liu YG, Li MQ, Liu HJ. Surface nanocrystallization and gradient structure developed in the bulk TC4 alloy processed by shot peening. *Journal of Alloys and Compounds*. 2016;685:186–193.
16. D1141-98 A Standard Practice for the Preparation

- of Substitute Ocean Water. ASTM International West Conshohocken. 2008.
17. Tao NR, Wang ZB, Tong WP, Sui ML, Lu J, Lu K. An investigation of surface nanocrystallization mechanism in Fe induced by surface mechanical attrition treatment. *Acta Materialia*. 2002;50:4603–4616.
 18. Sato M, Tsuji N, Minamino Y, Koizumi Y. Formation of nanocrystalline surface layers in various metallic materials by near surface severe plastic deformation. *Science and Technology of Advanced Materials*. 2004;5:145–152.
 19. Carrillo I, Valdez B, Zlatev R, Stoytcheva M, Carrillo M, Bäßler R. Electrochemical study of oxyanions effect on galvanic corrosion inhibition. *International Journal of Electrochemical Science*. 2012;7:8688–8701.
 20. Trachli B, Keddam M, Takenouti H, Srhiri A. Protective effect of electropolymerized 3-amino 1, 2, 4-triazole towards corrosion of copper in 0.5 M NaCl. *Corrosion Science*. 2002;44:997–1008.
 21. Yildiz R. An electrochemical and theoretical evaluation of 4, 6-diamino-2-pyrimidinethiol as a corrosion inhibitor for mild steel in HCl solutions. *Corrosion Science*. 2015;90:544–553.
 22. Dermaj A, Hajjaji N, Joiret S, Rahmouni K, Srhiri A, Takenouti H, Vivier V. Electrochemical and spectroscopic evidences of corrosion inhibition of bronze by a triazole derivative. *Electrochimica Acta*. 2007;52:4654–4662.
 23. Rammelt U, Schiller CA. Impedance studies of layers with a vertical decay of conductivity or permittivity. *ACH-Models in Chemistry*. 2000;137:199–212.
 24. Mi H. The corrosion behaviour of a low carbon steel in natural and synthetic seawaters. *Journal of the Southern African Institute of Mining and Metallurgy*. 2006;106:585–592.
 25. Trela J, Scendo M. Sodium molybdate (VI) as a corrosion inhibitor of carbon steel, *Technical Issues*. 2015;2:47–53.
 26. Lv J, Luo H. Comparison of corrosion behavior between coarse grained and nano/ultrafine grained 304 stainless steel by EWF, XPS and EIS. *Journal of Nuclear Materials*. 2014;452:469–473.
 27. Li W, Li DY. Influence of surface morphology on corrosion and electronic behavior. *Acta Materialia*. 2006;54:445–452.
 28. Moudgil HK, Yadav S, Chaudhary RS, Kumar D. Synergistic effect of some antiscalants as corrosion inhibitor for industrial cooling water system. *Journal of Applied Electrochemistry*. 2009;39:1339–1347.
 29. Refaey SAM, El-Rehim SSA, Taha F, Saleh MB, Ahmed RA. Ahmed, Inhibition of chloride localized corrosion of mild steel by PO_4^{3-} , CrO_4^{2-} , MoO_4^{2-} and NO_2^- anions. *Applied Surface Science*. 2000;158:190–196.
 30. Sanaty-Zadeh A, Raeissi K, Saidi A. An investigation on the effect of electrochemical adsorbates on properties of electrodeposited nanocrystalline Fe–Ni alloys. *International Journal of Nanoscience*. 2013;12:1350002.
 31. Nastasi M, Parkin DM, Gleiter H. Mechanical properties and deformation behavior of materials having ultra-fine microstructures. Springer Science & Business Media, 2012.
 32. Hempelmann R, Natter H. Nanostructured Metals and Alloys Deposited from Ionic Liquids. *Electrodeposition from Ionic Liquids*. 2008;222:213–238.
 33. Sommer WJ, Weck M. Facile functionalization of gold nanoparticles via microwave-assisted 1, 3 dipolar cycloaddition. *Langmuir*. 2007;23:11991–11995.